processes

MDPI

Article

Particle Migration Behavior of Coal Gasification Fine Slag During Spiral Chute Separation

Lijun Liu, Liang Han, Yushun Lin, Yizhe Yang, Bo Hu, Zhen Li, Wei Yu *, Songjiang Chen * and Ningning Zhang

School of Chemistry and Chemical Engineering, Xi'an University of Science and Technology, Xi'an 710064, China; liulijun@xust.edu.cn (L.L.); yyz2423941077@163.com (Y.Y.); m18190623629@163.com (B.H.)
* Correspondence: yuweiba@163.com (W.Y.); chen.songjiang@xust.edu.cn (S.C.)

Abstract

Coal gasification generates fine slag with high residual carbon, but its porous structure hinders efficient separation. This study investigates carbon–ash separation of gasification fine slag using a spiral chute. Particle size and pore structure jointly determine separation outcomes. Effective separation was achieved for +0.125 mm and 0.125–0.045 mm fractions, which exhibit developed porous carbon skeletons, yielding concentrate ash of 20.22% and 39.50%, respectively. Conversely, the −0.045 mm fraction (41.16% of feed) consists predominantly of mineral microspheres with poorly developed pores, leading to high feed ash (80.73%) and poor separation (concentrate ash 76.35%). Pore structure governs separation by reducing effective density through water absorption: high-porosity particles behave as light products and report to concentrate. Optimal conditions (10% concentration, 1.96 m^3/h) achieved 64.67% carbon recovery and 52.92% concentrate ash. A Bagnold-based model reveals that radial particle position is co-determined by effective density and particle size, with fine particle entrainment limiting separation precision.

Keywords: gasification slag; spiral chute; carbon/ash separation; porous structure; effective density; particle migration

1. Introduction

Coal gasification technology is a critical route for the production of clean energy and chemical feedstocks. However, the slag generated during this process poses a significant disposal challenge. Currently, gasification slag is primarily managed through landfilling or stockpiling, which not only wastes resources and contaminates the environment but also occupies substantial land area. When used in construction materials such as cement admixtures or bricks, the residual carbon in the slag tends to absorb moisture and chemical additives, thereby compromising product strength or causing volume instability [1–3].

Gasification slag is generally classified into two types: coarse slag and fine slag. The carbon content in coarse slag is typically below 10%, whereas fine slag contains a higher proportion of unburned carbon, generally ranging from 15% to 40%, along with abundant inorganic components. After carbon–ash separation, gasification fine slag exhibits potential for utilization as a secondary fuel, chemical feedstock, or construction material [4]. However, due to its porous structure and surface-rich oxygen-containing functional groups, efficient separation of gasification fine slag remains challenging. Therefore, developing an efficient and economically viable carbon–ash separation technology for gasification fine slag is of paramount importance for its high-value utilization and for advancing the sustainable development of the coal gasification industry. The annual generation

Check for updates

Academic Editor: Tiancheng Mu

Received: 4 August 2026
Revised: 23 August 2026
Accepted: 24 August 2026
Published: 25 August 2026

Copyright: © 2026 by the authors. Licensee MDPI, Basel, Switzerland. This article is an open access article distributed under the terms and conditions of the Creative Commons Attribution (CC BY) license.

of coal gasification slag in China exceeds 50 million tons, with fine slag accounting for approximately 20–30% of the total output due to entrainment in the syngas stream. The high residual carbon content and complex mineralogical composition of this fine slag make its disposal particularly challenging, as landfilling not only wastes valuable carbon resources but also poses environmental risks including heavy metal leaching and fugitive dust emissions [4].

Various methods, including flotation, gravity separation, and electrostatic separation, have been extensively employed for carbon–ash separation from gasification fine slag. Flotation, while exhibiting some efficacy in processing fine-grained materials, requires substantial quantities of collectors and other reagents due to the inherently high specific surface area and low hydrophobicity of gasification fine slag [5]. This requirement not only increases processing costs but also introduces the risk of secondary environmental pollution [6–8]. Gravity separation techniques, such as those utilizing shaking tables, offer high separation precision; however, they are often constrained by limited throughput and operational complexity.

The spiral chute, a gravity separation device operating on the principle of flowing film separation, offers distinct advantages including non-powered operation, high throughput, and low processing costs. It has been successfully applied in the separation of fine particles from ores such as iron ore and beach sand. Its separation performance is primarily governed by differences in particle settling velocity within the spiral chute, arising from the combined force field of gravity, centrifugal force, and fluid shear. This provides a theoretical basis for separating high-carbon and low-carbon components characterized by significant differences in separation density [9,10].

To date, research on spiral chutes has predominantly focused on conventional mineral systems, including the separation of ilmenite from quartz, wolframite from quartz, the desulfurization of coal slime [11–14], and the recovery of other resources [15]. Studies on the separation mechanism of spiral chutes have largely centered on optimizing operating parameters [16–18] and understanding particle motion laws [19]. Recent studies have demonstrated the viability of gravity separation, particularly using spiral concentrators, for processing gasification fine slag. Yu et al. [20] first reported the enrichment of residual carbon from such slag using a spiral separator, successfully producing a concentrate with acceptable ash content. Lv et al. [21] further improved carbon recovery by integrating gravity separation with flotation in a combined flowsheet. Comprehensive reviews by Ren et al. [3] and Matjie and Van Alphen [4] have summarized the mineralogical features and separation challenges of coal gasification slags, emphasizing the need for a more mechanistic understanding of particle behavior in gravity separators. Despite these advances, however, the fundamental migration behavior of porous slag particles within the spiral chute—particularly for fine slag with complex compositional heterogeneity—remains insufficiently understood, and the relationship between chute configuration, operating parameters, and separation mechanism has yet to be systematically elucidated.

Therefore, this study systematically investigates the separation performance of gasification fine slag in a spiral chute through coordinated regulation of feed concentration and flow rate, and elucidates the underlying particle separation mechanism. The distribution and migration behavior of particles with different sizes are analyzed, and the role of pore structure in governing particle migration via effective density modulation is revealed, with particular emphasis on the constraints imposed by fine particles on separation precision. These findings provide a new pathway for the low-cost and efficient separation of porous and complex components.

2. Materials and Methods

2.1. Test Raw Materials

The gasification fines used in this study were obtained from a fluidized bed gasification unit at the Future Energy Chemical Industry Co., Ltd., located in Yulin, Shaanxi Province, China. After sampling, they were first dried in a forced-air drying oven at 105 °C for 24 h until constant weight, to remove free moisture. Approximately 200 kg of raw fine slag was obtained, thoroughly mixed by the quartering method, and then divided into replicate sub-samples for subsequent experiments. All tests were performed in duplicate, and the average values were reported to minimize random errors.

2.2. Experimental Device and Procedures

The experimental setup primarily consisted of a mixing tank, control valves for feed stabilization, a spiral chute (600 mm in diameter, 240 mm pitch, 7 turns), and a collection trough. A schematic diagram of the experimental setup and process flow is shown in Figure 1. To achieve the desired feed concentration, predetermined amounts of dried gasification fines and water were weighed and mixed in the tank to prepare approximately 30 L of slurry, which was continuously agitated vigorously for 15 min to ensure complete wetting and homogeneity. The flow rate was precisely adjusted to the set value via the control valve, after which the slurry was fed into the center at the top of the spiral chute. Once a stable flowing film had developed, samples of the concentrate, middlings, and tailings were collected at the bottom discharge outlet. Each product was subsequently filtered, dried, and weighed, and the mass of each fraction was recorded. All experiments were conducted in duplicate, and the average value was reported. If the deviation between the two measurements exceeded 5%, an additional test was performed.

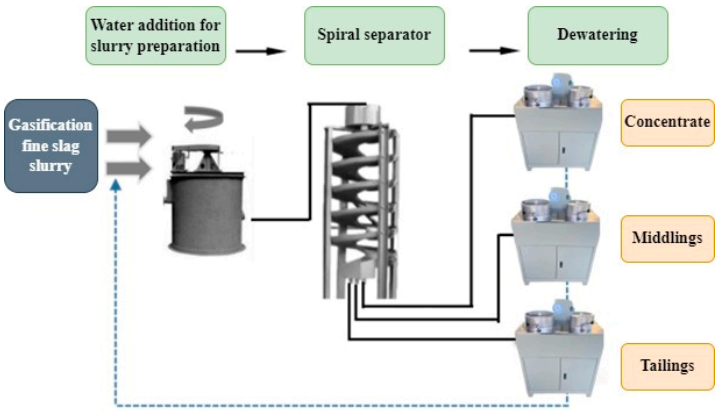

Figure 1. Schematic of the spiral sorting system.

2.3. Analytical Methods and Evaluation Indicators

2.3.1. Analytical Methods

The mineral compositions of the raw sample, its size-fractionated samples, and the separated product samples were determined using an X-ray diffraction (XRD) analyzer (model D8 Advance, Bruker; Billerica, MA, USA). The analysis was conducted with Cu Kα radiation (λ = 1.5418 Å) at a voltage of 40 kV and a current of 40 mA. Scanning was performed over a 2θ range from 5° to 80° with a step size of 0.02°.

The pore size and specific surface area of the raw sample, its size-fractionated samples, and the separated product samples were measured using a physical adsorption instrument (ASAP2020, Micromeritics; Norcross, GA, USA).

Morphological observations of the raw sample, its size-fractionated samples, and the separated product samples were conducted using a scanning electron microscope (SEM, model JSM 6460LV, JEOL; Akishima, Tokyo, Japan).

Proximate analysis of the raw sample, its size-fractionated samples, and the separated product samples was performed following the Chinese standard GB/T 212-2008 Proximate Analysis of Coal. Proximate analysis of the raw sample, its size-fractionated samples, and the separated product samples was conducted according to the Chinese national standard GB/T 212-2008 (*Proximate Analysis of Coal*).

All experimental data were processed and analyzed using OriginPro 2021 (OriginLab Corporation, Northampton, MA, USA). Figures were prepared using Microsoft PowerPoint (Microsoft Corporation, Redmond, WA, USA), and the manuscript was written using Microsoft Word (Microsoft Corporation, Redmond, WA, USA).

2.3.2. Evaluation Indicators

The residual carbon recovery rate was used to evaluate the recovery performance of the spiral chute separation [21], indicating the proportion of fixed carbon recovered from the raw slag relative to the total fixed carbon in the raw slag. The calculation formula is

$$\varepsilon_v = \frac{\gamma_c \times (100 - A_c) \times 100\%}{100 - A_v} \quad (1)$$

where ε_v represents the carbon recovery rate (%), γ_c represents the yield of the concentrate (%), A_c represents the ash content of the concentrate (%), and A_v represents the ash content of the original gasification fine slag (%).

The sorted products were wet-sieved into three size fractions (+0.125 mm, 0.125–0.045 mm, and −0.045 mm) to obtain the particle size distribution. Particle migration behavior during the spiral separation process was analyzed using the particle size distribution rate as an indicator:

$$D_{j,i} = \frac{\gamma_j \times \gamma_{j,i}}{\gamma_{0,i}} \times 100\% \quad (2)$$

The distribution rate $D_{j,i}$ (%) of materials entering the ith product (such as concentrate, middlings, or tailings) at grain size level j. γ_j represents the yield of the jth product. $\gamma_{j,i}$ represents the yield of the product with grain size level i in the jth product. $\gamma_{0,i}$ represents the yield of the product with grain size level j in the raw material.

3. Results

3.1. Raw Material Characteristics

3.1.1. Material Composition and Proximate Analysis

The results of the proximate analysis, conducted in accordance with GB/T 212-2008, are presented in Table 1.

Table 1. Proximate analysis of gasification fine slag.

Proximate Analysis/%				Element Content/%				
M_{ad}	A_{ad}	W_{ad}	FC_{ad}	C_{daf}	H_{daf}	O_{daf}	N_{daf}	S_{daf}
2.05	66.37	2.36	29.22	37.84	0.67	5.90	0.17	0.35

As shown in Table 1, the gasification fine slag exhibited a fixed carbon content (FC_{daf}) of 29.22%, which is considerably high, indicating that the residual carbon components are valuable and worthy of separation and recovery.

The particle size composition of the gasification fine slag was determined according to GB/T 477-2008, as shown in Table 2.

Table 2. Particle size analysis of gasification fine slag.

Particle Size/mm	Weight/g	Yield/%	Ash Content/%	Screened Cumulative/%		Filtered Cumulative/%	
				Yield	Ash Content	Yield	Ash Content
+0.5	13.35	6.63	69.63	6.63	69.63	100.00	66.37
0.5~0.25	30.29	15.05	33.64	21.69	44.65	93.37	66.13
0.25~0.125	28.66	14.24	46.17	35.93	45.26	78.31	72.38
0.125~0.075	25.45	12.65	69.09	48.58	51.46	64.07	78.20
0.075~0.045	20.65	10.26	79.32	58.84	56.32	51.42	80.44
−0.0450	82.83	41.16	80.73	100.00	66.37	41.16	80.73
Total	201.23	100.00	66.37				

The particle size composition of the gasification fine slag was determined according to the Chinese national standard GB/T 477-2008 (*Method for Size Analysis of Coal*), as shown in Table 2.

The ash content of each size fraction, as presented in Table 2, shows a clear increasing trend with decreasing particle size, with the −0.045 mm fraction reaching the highest ash content of 80.73%. The +0.125 mm fractions exhibit relatively lower ash contents and well-developed porous carbon skeletons, making them amenable to spiral separation.

The particle size distribution of the raw gasification fine slag is presented as cumulative curves in Figure 2.

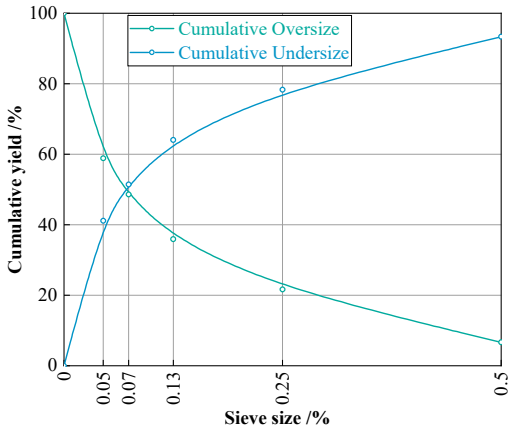

Figure 2. Particle size distribution curves of raw gasification fine slag.

The curve shows that the −0.045 mm fraction accounts for 41.16% of the total mass, confirming its dominance in the size distribution. The d50 and d80 values, determined from the screened cumulative curve, are approximately 0.058 mm and 0.42 mm, respectively. The high proportion of fine particles with elevated ash content constitutes the core bottleneck for effective spiral separation.

The X-ray diffraction analysis of the gasification fine slag is shown in Figure 3.

As shown in Figure 3a, the XRD analysis identifies quartz, mullite, and calcite as the primary crystalline phases in gasification fine slag. Figure 3b reveals that the amorphous hump area increases with particle size, suggesting a higher proportion of amorphous phases (including both unburned carbon and aluminosilicate glass) in coarser fractions. It should be noted that the amorphous hump cannot be used for quantitative carbon estimation, as it originates from both carbonaceous and glassy components. The peak

at 26.6° corresponds to both quartz and graphitized carbon, consistent with decreasing ash content as particle size increases. Mineral distribution varies across fractions: the −0.045 mm fraction is quartz-enriched; calcite concentrates in the 0.125~0.5 mm range; mullite is uniformly distributed.

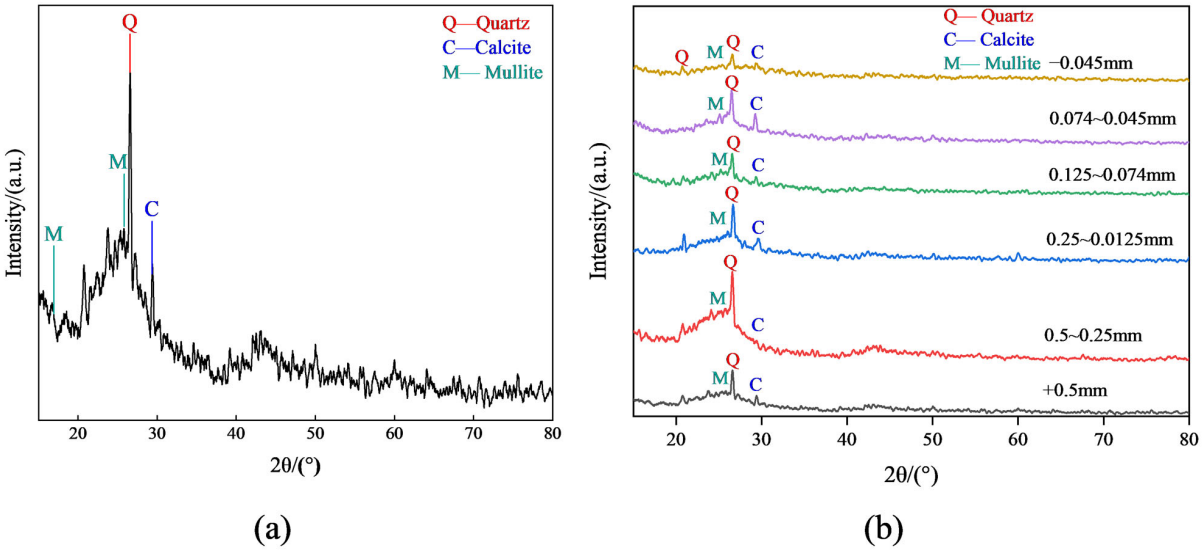

Figure 3. XRD patterns of (**a**) raw gasification fine slag and (**b**) different particle size fractions.

The XRD analysis reveals that the primary crystalline mineral phases in gasification fine slag are quartz, mullite, and calcite. As particle size increases, the content of amorphous phases increases, while fine fractions are more enriched in crystalline minerals such as quartz. This difference in mineral distribution across particle sizes significantly influences the spiral separation process: coarse particles, with higher amorphous carbon content and lower ash, tend to report to the concentrate, whereas fine particles (−0.045 mm), dominated by high-ash crystalline minerals, constitute the main factor limiting separation precision.

3.1.2. Morphological Features and Pore Structure Analysis

The raw gasification fine slag and its size-fractionated samples are shown in Figure 4, with the raw material presented in Figure 4a. As observed in Figure 4b, the surface exhibits larger pores with attached microspheres and crystalline fragments displaying a reflective transparent luster. This morphology is attributed to the transformation of clay minerals such as kaolinite, illite, and montmorillonite, as well as other aluminosilicates present in the raw coal, which form stable crystalline phases, primarily mullite, at the high temperatures within the gasification furnace. Alternatively, these minerals may form low-temperature eutectics with oxides containing Fe, Ca, K, Na, and other elements. Concurrently, silicon dioxide reacts with alkaline earth metal oxides under high-temperature conditions to form silicates, thereby participating in the reaction process [1].

As shown in Figure 4c–h, the SEM analysis reveals that the morphology of gasification fine slag exhibits regular variations with decreasing particle size: +0.5 mm particles possess developed pores but some voids are filled with fine particles, resulting in slightly higher ash content; 0.5~0.125 mm particles show uniform and regular surface pores with few fillings and lower ash content; −0.045 mm particles are mainly composed of debris and microspheres with underdeveloped pore structures, exhibiting the highest ash content of 80.73%. Consequently, during spiral chute separation, 0.5~0.125 mm particles, characterized by clear pore structures and clean surfaces, facilitate density differentiation within the flowing film and achieve effective separation. In contrast, −0.045 mm fine particles, lacking

a porous carbon skeleton and dominated by high-ash minerals, are prone to entrainment by fluid flow into the concentrate, constituting the core factor limiting separation precision.

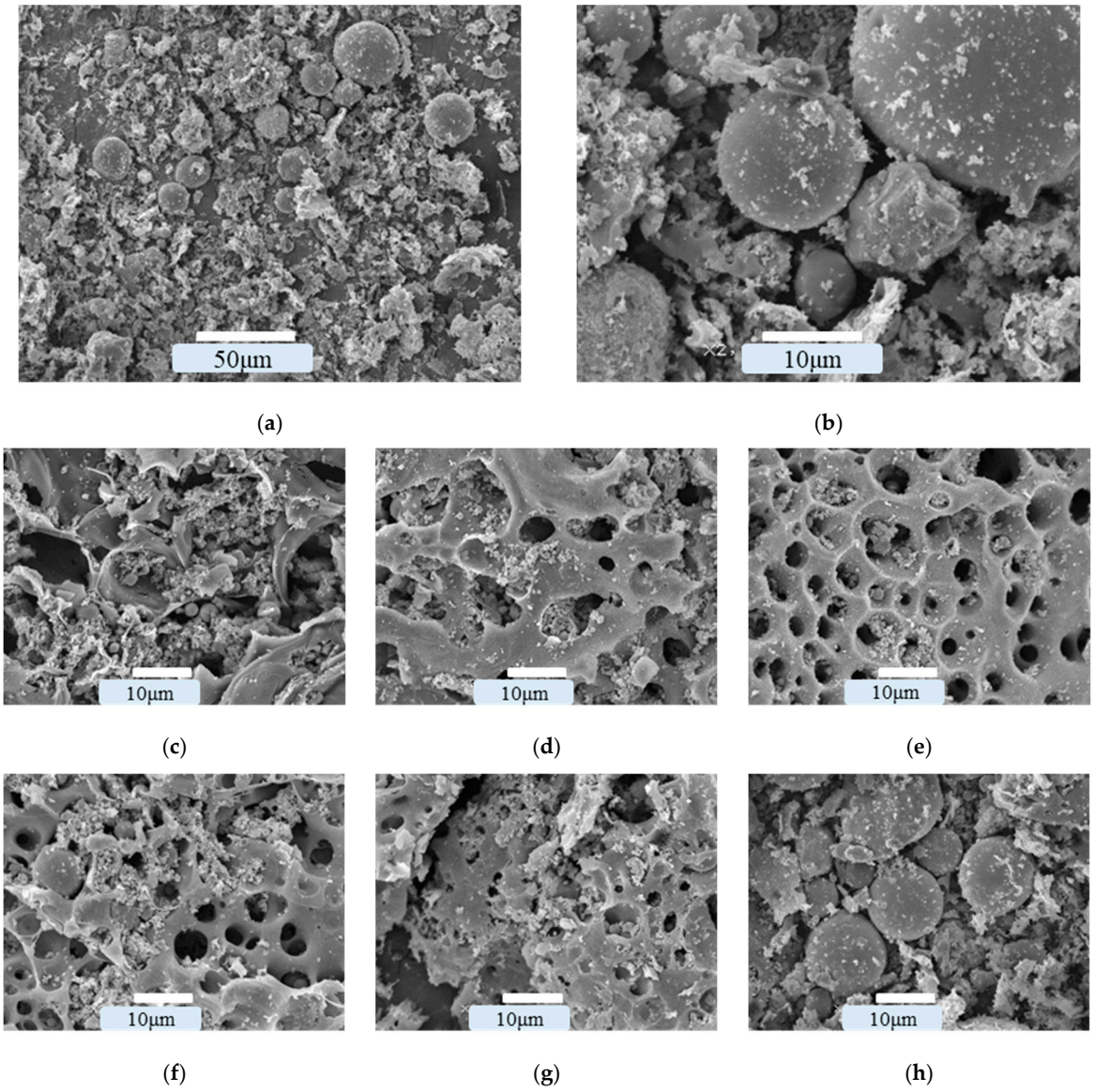

Figure 4. SEM images of different grain sizes in original form. (**a**) As-received; (**b**) as-received; (**c**) +0.5 mm; (**d**) 0.5~0.25 mm; (**e**) 0.25~0.125 mm; (**f**) 0.125~0.074 mm; (**g**) 0.074~0.045 mm; (**h**) −0.045 mm.

Nitrogen adsorption measurements were performed on the size-fractionated samples, and the pore size distributions were calculated based on the corresponding adsorption isotherms. The results for different particle size fractions are presented in Figure 5.

As shown in Figure 5a, the physical adsorption isotherm of the gasification fine slag exhibits a Type IV(a) isotherm. The adsorption behavior of this mesoporous material is governed by both the interaction between the adsorbent and adsorbate and the intermolecular interactions within the condensed phase. The hysteresis loop observed in the adsorption–desorption isotherm corresponds to the H3 type, which is influenced by adsorption metastability and the networked molecular structure. This type of hysteresis is typically associated with aggregates having layered structures, leading to the formation of slit-shaped mesopores [22,23]. The original gasification fine slag possess a specific surface area of 207.25 m^2/g, a total pore volume of 0.23 cm^3/g, and an average pore diameter of

4.98 nm. According to the IUPAC classification established in 1985, the gasification fine slag is categorized as a mesoporous material, with pore widths ranging from 2 to 50 nm. Clay minerals such as kaolinite are inherently layered silicates; upon solidification, they form a layered structure comprising alternating glassy and carbon phases, a feature that is corroborated by SEM observations [24,25].

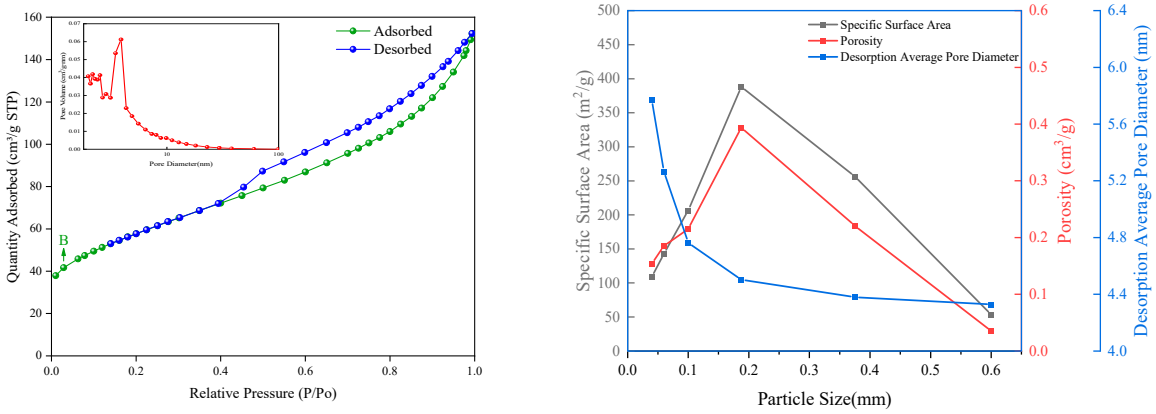

(**a**) (**b**)

Figure 5. Adsorption isotherms of gasification slag and pore size curves calculated from adsorption curves of gasification slag samples with different particle sizes.

As shown in Figure 5b, with decreasing particle size, both the specific surface area and porosity of the gasification fine slag exhibit an initial increase followed by a decrease. The maximum values are observed in the 0.25~0.125 mm fraction, with a specific surface area of 388.02 m^2/g and a porosity of 0.39 cm^3/g. The average pore diameter increases as particle size decreases, rising from 4.98 nm to 5.77 nm, and all fractions remain within the mesoporous range. During spiral chute separation, particles with high specific surface area and abundant mesopores experience a significant reduction in effective density due to water infiltration into the pores. Consequently, these particles encounter greater viscous resistance within the flow, which adversely affects separation precision. Furthermore, porous and brittle particles are more susceptible to fragmentation and abrasion during separation, thereby influencing their lateral migration and vertical settling behavior in the flowing film of the spiral chute.

The material characterization presented above also provides the basis for equipment selection. For gasification fine slag, the effective density contrast between porous carbon-rich particles and dense mineral particles exceeds 0.5 g/cm^3 for the +0.125 mm and 0.125–0.045 mm fractions, confirming the theoretical feasibility of gravity separation. The spiral chute was therefore selected as the separation device, as it offers high throughput, low operating cost, and reagent-free operation, making it particularly suitable for processing low-value gasification slag.

3.2. Effects of Flow Rate and Concentration on Separation Performance

3.2.1. Effect of Feed Flow Rate

Separation experiments were performed using a spiral chute (600 mm in diameter, 240 mm pitch, 7 turns). The variations in concentrate ash content and carbon recovery rate as a function of feed flow rate, at a constant feed concentration of 10%, are illustrated in Figure 6.

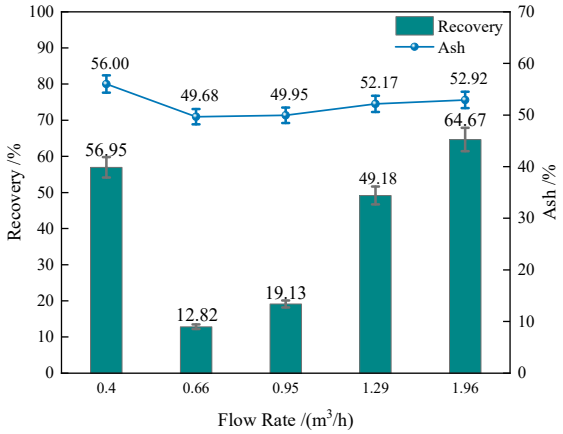

Figure 6. Recovery rate of gasification slag at different feed flow rates.

Figure 6 illustrates the variation in carbon recovery rate during spiral separation of gasification fine slag as a function of feed flow rate. Overall, the carbon recovery rate exhibits a marked increase with rising feed flow rate.

At low flow rates (0.40~0.66 m^3/h), the turbulence intensity of the pulp is weak, resulting in poor particle dispersion and slow stratification of heavy and light minerals. Under these conditions, residual carbon is readily entrained and settles, leading to low recovery rates. As the flow rate increases to 0.95 m^3/h, the enhanced shear force accelerates particle stratification and enables rapid enrichment of residual carbon on the chute surface, yielding a recovery of 56.95%. However, when the flow rate is further increased to 1.29 m^3/h, the recovery drops sharply to 12.82%, which is attributed to a critical mismatch between film thickness and particle settling velocity at this specific flow rate, where intensified turbulence causes re-mixing of stratified particles and carbon entrainment into the inner trough. At 1.96 m^3/h, the flow transitions to a stable turbulent regime where centrifugal stratification dominates, and the recovery rises to 64.67%. These observations indicate that feed flow rate influences recovery by modulating the shear force within the pulp and the efficiency of particle stratification. At a feed flow rate of 1.96 m^3/h, the residual carbon recovery reaches a maximum of 64.67%, with a corresponding concentrate ash content of 52.92%, identifying this as the optimal operating condition for the spiral chute of the given configuration at a feed concentration of 10%.

3.2.2. Effect of Feed Concentration

The variation in carbon recovery rate of gasification fine slag with feed concentration, at feed flow rates of 0.40, 0.66, 0.95, 1.29, and 1.96 m^3/h, is presented in Figure 7.

As shown in Figure 7, at feed flow rates of 0.40~0.66 m^3/h, the carbon recovery rate decreases with increasing feed concentration and remains at a low level. Under low flow rate conditions, particle stratification proceeds slowly, and the increase in concentration further impairs separation efficiency, resulting in a consistently low and continuously declining recovery rate. At feed flow rates of 0.95~1.96 m^3/h, the carbon recovery rate initially increases and then decreases with rising feed concentration, reaching a maximum at a feed concentration of 15%. At higher flow rates, the turbulence intensity of the pulp is enhanced, leading to a greater velocity differential between particles. Once heavy and light minerals are effectively dispersed, efficient separation occurs. Consequently, the carbon recovery rate increases as the feed concentration rises from 10% to 15%. However, when the concentration increases further from 15% to 20%, the carbon recovery rate declines, with the extent of this decrease diminishing as the flow rate increases.

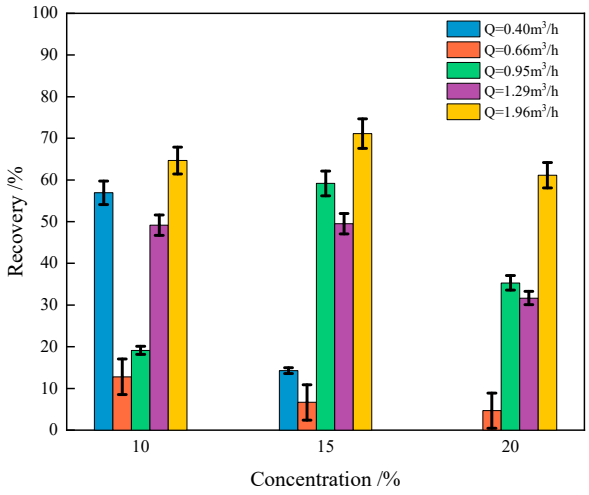

Figure 7. Recovery rate of gasification fine slag at different concentrations.

Based on the separation performance of gasification fine slag in the spiral chute under varying flow rate and concentration conditions, a significant synergistic effect between feed concentration and flow rate is observed. This effect is characterized by a decrease in carbon recovery rate with increasing concentration at low flow rates, and an initial increase followed by a decrease at high flow rates. The distribution and migration of the different particle sizes of the gasification slag and the influence of the gasification slag pores on the chute separation process are discussed in the next chapter.

4. Discussion

4.1. Conceptual Flowsheet and Separation Mechanism

Figure 8 presents the conceptual flowsheet and radial separation mechanism of gasification fine slag in the spiral chute. Panel (a) shows the process flowsheet from feed classification to product streams, and panel (b) illustrates the particle migration mechanism on a radial cross-section of the spiral trough.

The feed material is primarily composed of porous carbonaceous particles and dense mineral microspheres, with the −0.045 mm fraction accounting for 41.16% of the total feed. Separation is conducted using a spiral chute with a diameter of 600 mm, a pitch of 240 mm, and 7 turns. Under the optimal operating conditions of 10% solids concentration and 1.96 m^3/h feed rate, the products are classified into concentrate, middlings, and tailings. The concentrate achieves an ash content of 20.22% and a carbon recovery of 64.67%, while the tailings exhibit an ash content exceeding 80%. Secondary circulation drives the upper film flow radially outward and the lower film flow inward. The high shear rate near the inner trough generates the Bagnold effect, promoting vertical particle stratification. Porous carbon particles, after water absorption, exhibit a markedly reduced effective density and migrate to the outer trough for collection as concentrate. In contrast, dense ash particles with high effective density settle toward the inner trough and report to the tailings. For fine particles below 0.045 mm, the absence of a well-developed porous structure eliminates their effective density advantage over mineral components, resulting in these particles being readily entrained by the upper fluid flow into the concentrate stream, with a concentrate ash content as high as 76.35% for this size fraction.

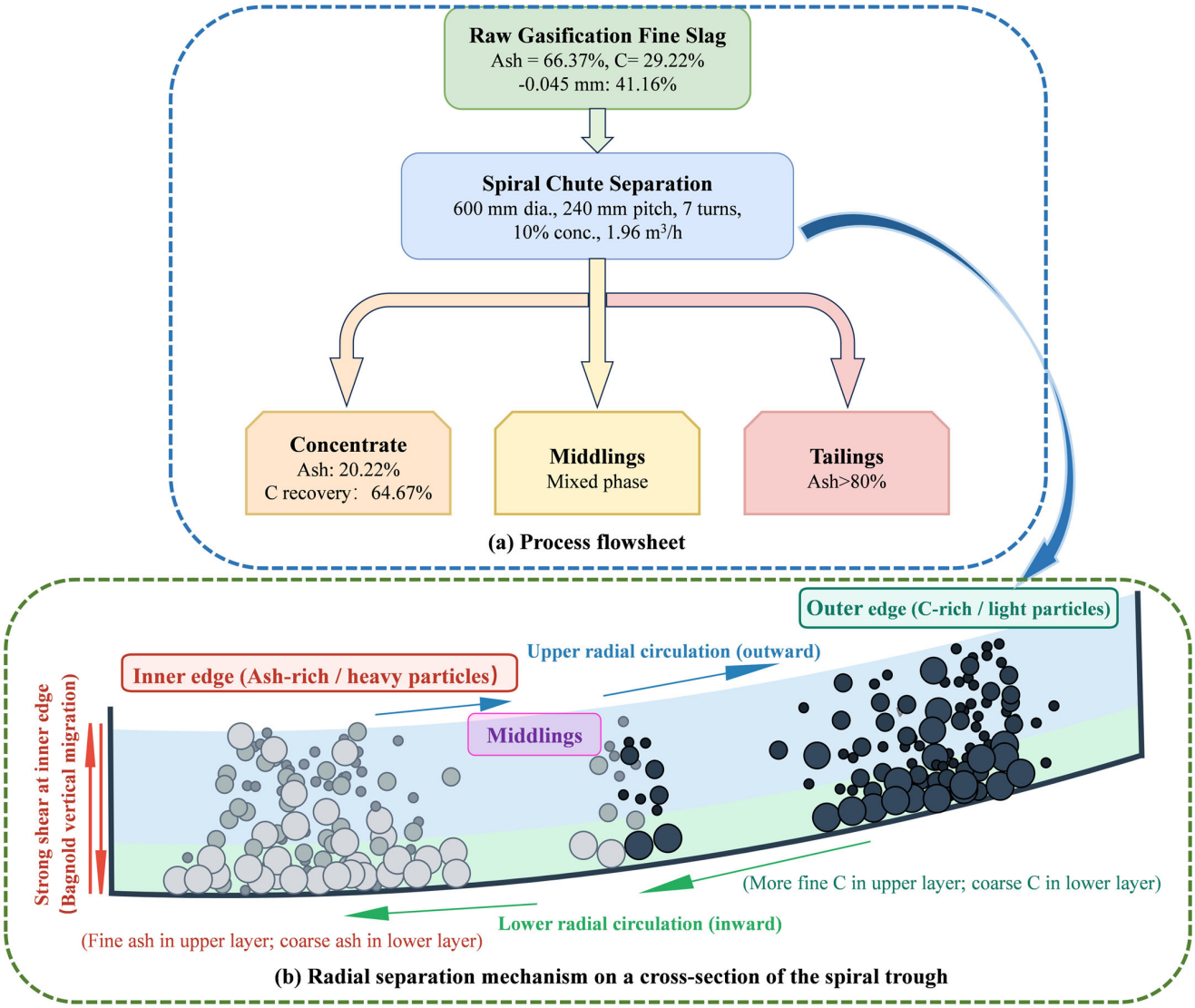

Figure 8. Conceptual flowsheet and radial separation mechanism of gasification fine slag in a spiral chute.

4.2. Particle Migration Behavior

Figure 9 presents the particle distribution rates obtained at various feed flow rates under a constant feed concentration of 10%. The particle size distributions of the concentrate, middlings, and tailings products were analyzed to investigate the particle migration behavior during spiral separation of gasification fine slag.

Based on the particle size characteristics of the raw material, the content of the −0.045 mm fraction is relatively high. Given its significance as an influencing factor, this fine fraction was selected as a distinct group for analysis. For the remaining size fractions, the yield and ash characteristics of the raw material were considered, with 0.125 mm identified as a key particle size threshold for evaluation.

As shown in Figure 9, the feed flow rate significantly influences the particle size distribution of products obtained from spiral separation of gasification fine slag. The distribution rates of the +0.125 mm, 0.125–0.045 mm, and −0.045 mm fractions in the concentrate all exhibit a trend of initially decreasing and then increasing with increasing flow rate. The probability of fine particles entering the concentrate increases, and the carbon recovery rate reaches the highest value of 64.67% at 1.96 m^3/h, with an ash content of 52.92%. However, ash contamination also intensifies. The distribution rates of each particle size in the middlings all decrease with increasing flow rate and gradually tend to

become consistent, reflecting that the radial velocity gradient increases after the flow rate increases, the separation of heavy and light minerals intensifies, and the probability of all particle sizes entering the middlings zone decreases. The distribution rates of each particle size in the tailings all rapidly increase first and then slowly decrease with increasing flow rate. At low flow rates, the distribution rate of −0.045 mm fine particles is higher than that of +0.125 mm coarse particles, and vice versa at high flow rates. Under high flow rate conditions, coarse particles with low ash content tend to report to the tailings, resulting in carbon loss.

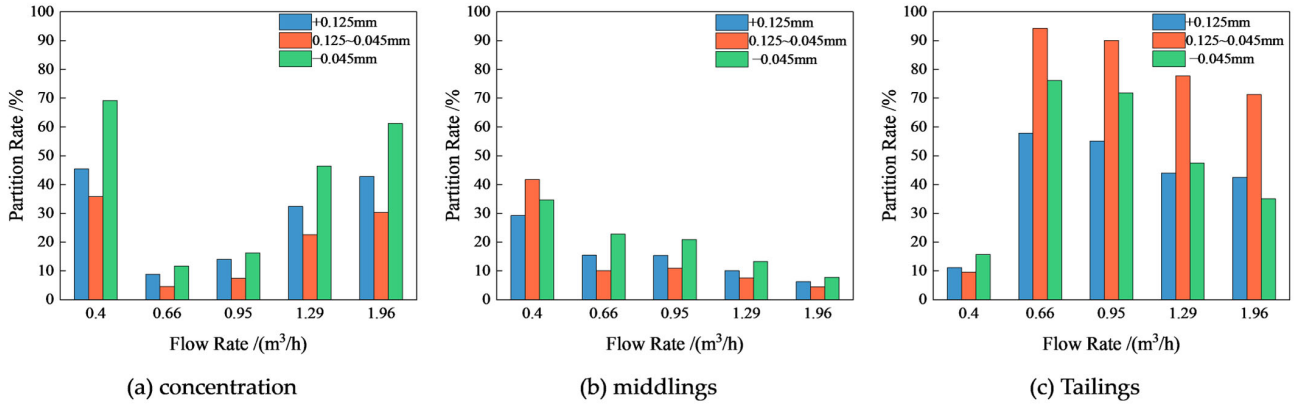

Figure 9. Partition rate of gasification fine slag under different feed flow rates. (**a**) Concentration; (**b**) middlings; (**c**) tailings.

The particle size distribution rates for each product show that in the concentrate and middlings, $\varepsilon_{-0.045} > \varepsilon_{+0.125} > \varepsilon_{0.125\sim0.045}$, while in the tailings, $\varepsilon_{0.125\sim0.045} > \varepsilon_{-0.045} > \varepsilon_{+0.125}$. Combined with the characteristics of the raw sample, the particle size distribution on the chute surface shows a clear feature: the heavy products near the inner edge are mainly −0.125 mm high-ash fine mud, the middle zone is mainly −0.045 mm and +0.125 mm particle sizes, and the light products near the outer edge are mainly +0.125 mm low-ash coarse particles and −0.045 mm fine particles. The migration of low-ash coarse particles into the concentrate is accompanied by significant entrainment of fine particles, resulting in contamination of the concentrate product.

In summary, as the feed flow rate increases, the tendency for coarse particles to report to the concentrate becomes more pronounced, although a portion of coarse particles continues to be lost to the tailings. Concurrently, the proportion of high-ash fine particles decreases in the tailings and increases in the concentrate, with their excessive migration constituting the primary factor contributing to the elevated ash content in the concentrate. To reduce the concentrate ash content, optimization is required in three key aspects: first, minimizing the proportion of high-ash fine particles; second, selecting the optimal feed flow rate; and third, mitigating the excessive migration of fine particles by reducing the number of separation stages.

4.3. Characterization of Product Distribution and Migration Behavior

The size fractions of the separated products obtained at a feed concentration of 10% and an optimal feed flow rate of 1.96 m^3/h were characterized by scanning electron microscopy, nitrogen adsorption, and X-ray diffraction analysis. By analyzing the morphology, surface area, pore size, and mineral composition of different particle size products of the sorted concentrate, middlings, and tailings, the distribution and migration behavior of the gasification fine slag in the spiral chute were revealed.

4.3.1. Morphology of Separated Products

Figure 10 shows the particle morphology of products sorted at different particle sizes.

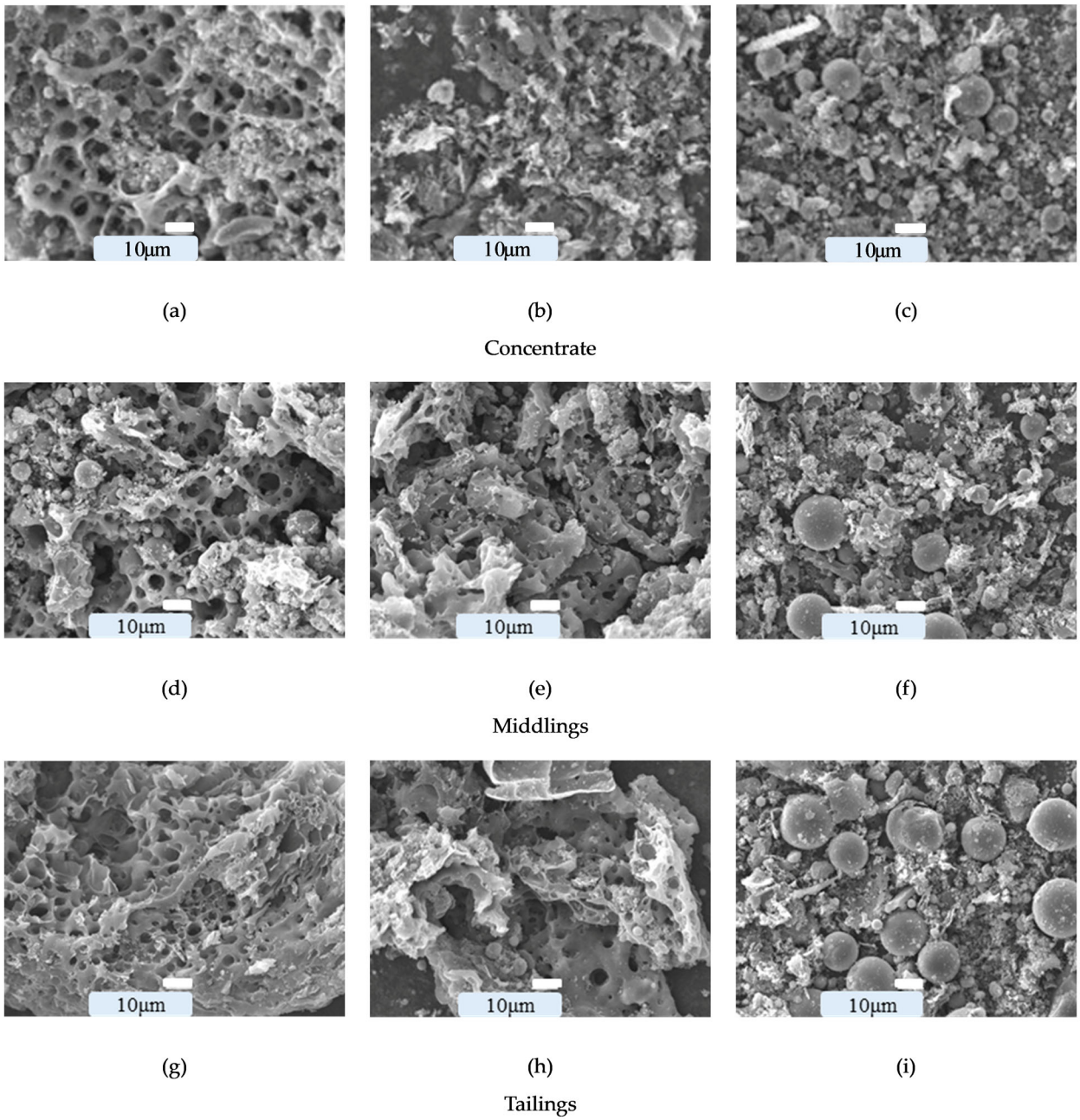

Figure 10. SEM images of separated products at different particle size fractions. (**a**) +0.125 mm; (**b**) 0.125~0.045 mm; (**c**) −0.045 mm; (**d**) +0.125 mm; (**e**) 0.125~0.045 mm; (**f**) −0.045 mm; (**g**) +0.125 mm; (**h**) 0.125~0.045 mm; (**i**) −0.045 mm.

As shown in Figure 10, the gasification fine slag samples are primarily composed of four distinct particle types: porous irregular particles, flocs, spherical fine particles, and isolated large spherical particles [26]. The particle morphology of the concentrate, middlings, and tailings is strongly associated with ash content. The clarity of the carbon skeleton in the concentrate decreases with decreasing particle size, the amount of mineral attachment gradually increases, and ash content increases significantly. The morphology of the middlings is similar to that of the concentrate; however, the extent of mineral encapsulation and adhesion on the carbon skeleton surface is more pronounced, resulting in a slightly

higher ash content compared to the concentrate. In contrast, the tailings are predominantly composed of the mineral phase, with the carbon skeleton being extensively covered or encapsulated. The ash content across all particle sizes in the tailings is substantially higher than that of both the concentrate and middlings. Additionally, notable differences are observed in the occurrence forms of minerals across different particle size fractions.

Figure 10a–c show the morphological characteristics of the concentrate at different particle sizes. For the +0.125 mm particle size (Figure 10a), a well-developed porous carbon skeleton structure is presented, with clear pore sizes and a clean surface. Only a small amount of scattered flocculent material is visible, corresponding to an ash content of 20.22%. Figure 10b shows that the 0.125–0.045 mm particle size still exhibits a sheet-like carbon skeleton, but the surface begins to adhere spherical mineral particles, and the amount of mineral attachment is significantly increased compared to the coarse particle size. Figure 10c shows that the porous carbon structure at the −0.045 mm particle size has completely disappeared, being fully covered by flocculent minerals and spherical microspheres, with the ash content abruptly rising to 76.35%.

Figure 10d–f show the morphological characteristics of the middlings at different particle sizes. Figure 10d shows that the carbon skeleton at the +0.125 mm particle size is still intact, but a small amount of glassy microspheres are attached to the surface. The bonding sites of the framework structure are more numerous, and the ash content is relatively low. Figure 10e shows that the surface of the 0.125–0.045 mm fraction is densely covered with fine-grained, glassy spheroidal minerals. Figure 10f shows that the −0.045 mm particle size contains various sizes of glass microspheres, as well as various fine-grained flocculent structures, with a higher ash content.

Figure 10g–i show the morphological characteristics of tailings at different particle sizes. Figure 10g shows that the +0.125 mm particle size carbon framework is tightly enclosed by sheet-like minerals, and there are a large number of fractures formed by melting and cooling. Figure 10h shows that the 0.125–0.045 mm particle size only has a thin carbon framework, with glass microspheres and flocculent minerals adhering to the surface. Figure 10i shows that the −0.045 mm particle size exhibits a dense distribution of 15 μm level spherical mineral aggregates, with the carbon framework completely invisible.

In summary, the +0.125 mm and 0.125–0.045 mm particle sizes, with their clear porous carbon skeletons, achieve effective separation in the spiral chute based on the degree of mineral attachment on the surface. The particle sizes entering the tailings have a significantly higher ash content due to the dense mineral encapsulation. In contrast, the −0.045 mm fine particles lack an obvious porous carbon structure, being primarily composed of mineral microspheres and flocs. Variations in ash content among different products are minimal, and the ash content of this fraction in the concentrate remains relatively high, which constitutes a critical bottleneck limiting separation efficiency. To further upgrade the residual carbon, targeted removal of the high-ash fine particle components (<0.045 mm) from the concentrate is necessary.

4.3.2. Mineral Composition of Separated Products

The XRD patterns of different particle size fractions of the separated products are shown in Figure 11, providing qualitative analysis of the mineral phases present. Combined with the morphological information obtained from SEM, it is evident that the mineral compositions of the concentrate and middlings across various particle sizes are essentially consistent. Both the +0.125 mm fractions of the concentrate and middlings contain a large area of amorphous phase humps, indicating a high content of amorphous carbon. The difference lies in the fact that the +0.125 mm fraction of the middlings also contains a certain amount of calcite and mullite, which is the fundamental reason for the higher ash content

of the middlings, at +0.125 mm, compared to the concentrate, at +0.125 mm. While the XRD patterns of the concentrate and middlings from 0.125 to 0.045 mm are very similar, the ash difference between the two is within 1%. The −0.045 mm gasification fine slag in the concentrate, middlings, and tailings exhibits a distinct quartz peak, and the peak areas are basically consistent, indicating that the spiral chute does not effectively separate the −0.045 mm gasification fine slag. The +0.125 mm fraction of the tailings shows a clear quartz peak, and the area of the amorphous hump is smaller than that of the middlings and concentrate at this particle size, indicating a lower content of amorphous carbon and a higher mineral content in this fraction, with ash content reaching 74.91%.

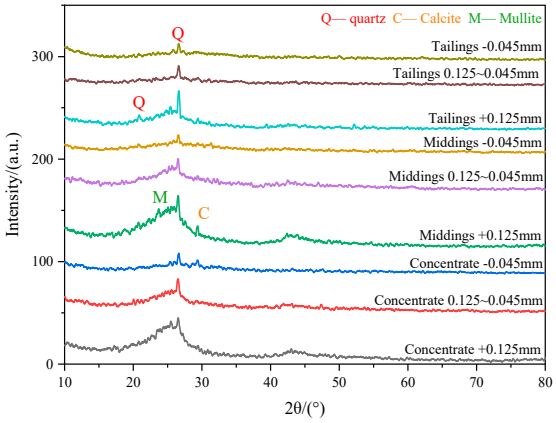

Figure 11. XRD patterns of products sorted at different particle size fractions.

In summary, effective separation of gasification fine slag in the spiral chute is achieved for the +0.125 mm and 0.125−0.045 mm fractions, whereas no significant separation is observed for the −0.045 mm fraction.

4.3.3. Surface Morphology and Pore Structure Characteristics

The specific surface areas (SBET) of different particle size fractions of the separated products are presented in Figure 12a. The average pore diameters (dp) and porosities of these fractions are shown in Figure 12b,c.

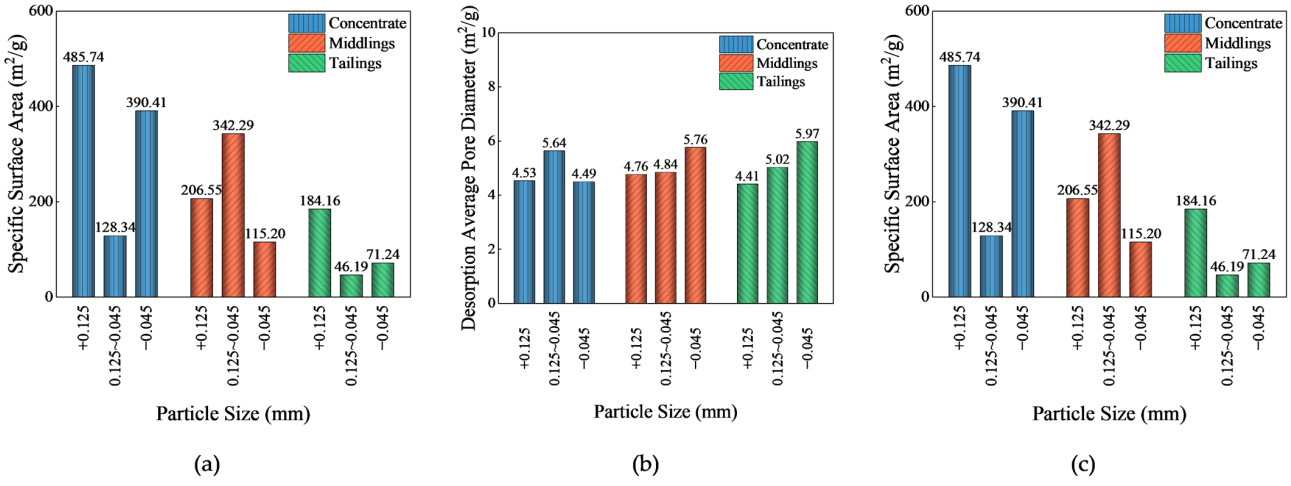

Figure 12. Surface morphology and pore size characteristics of gasification fines products. (**a**) Specific surface area of separated products sorted at different particle size fractions; (**b**) average pore diameter of separated products at different particle size fractions; (**c**) porosity of separated products at different particle size fractions.

As shown in Figure 12a, the specific surface areas of different particle size fractions of the separated products exhibit distinct trends. For the concentrate, the specific surface area follows the order $S_{+0.125} > S_{-0.045} > S_{0.125\sim0.045}$. For the middlings, $S_{0.125\sim0.045} > S_{+0.125} > S_{-0.045}$. For the tailings, $S_{+0.125} > S_{-0.045} > S_{0.125\sim0.045}$. Integrating the aforementioned analysis of product yield and quality with the SEM morphological observations, it is evident that the concentrate and middlings share similar morphological characteristics, with ash content primarily governed by the carbon framework. In contrast, the tailings are predominantly mineral-based, exhibiting high ash content. The concentrate and middlings possess higher specific surface areas overall, with the +0.125 mm fraction of the concentrate achieving the highest value of 485.74 m^2/g, attributable to minimal clay mineral attachment on the carbon framework and unobstructed pore structures. Conversely, the 0.125–0.045 mm fraction of the tailings exhibits the lowest specific surface area (46.19 m^2/g), consistent with its low residual carbon content and high mineral matter.

As shown in Figure 12b, the average pore diameters of the gasification fine slag range from 4 to 6 nm, classifying them as mesoporous materials. For the concentrate, the average pore diameter follows the order $Dp_{0.125\sim0.045} > Dp_{+0.125} > Dp_{-0.045}$. In contrast, the middlings and tailings exhibit the same trend with respect to particle size: $Dp_{-0.045} > Dp_{0.125\sim0.045} > Dp_{+0.125}$. Specifically, in the separated products, the concentrate exhibits a $Dp_{+0.125}$ of 4.53 nm and a $Dp_{-0.045}$ of 4.49 nm, whereas the tailings show a $Dp_{+0.125}$ of 4.41 nm and a $Dp_{-0.045}$ of 5.97 nm. These results indicate that during spiral separation, coarse particles with larger pore diameters preferentially migrate to the outer edge of the concentrate, while those with smaller pore diameters tend to report to the inner edge of the tailings. Furthermore, fine particles with smaller pore diameters are prone to entering the concentrate zone, resulting in high-ash fine mud contamination. Conversely, only fine particles with larger pore diameters are directed to the tailings zone.

The porosity of products obtained from different particle size fractions after separation is presented in Figure 12c. The trend in total pore volume (Vt) is consistent with that of the specific surface area. The SEM image analysis of the separated size fractions reveals that the +0.125 mm fraction of the concentrate exhibits the highest total pore volume (0.48 cm^3/g), indicating significant enrichment of carbon particles in this fraction. Following spiral separation, minimal clay mineral attachment is observed, with clean pore structures clearly visible. This demonstrates the effectiveness of the spiral chute in achieving carbon–ash separation for such high-porosity materials. In contrast, the −0.045 mm fraction of the tailings shows a low total pore volume of 0.10 cm^3/g, suggesting that fine particles with low porosity are preferentially directed to the tailings zone. The underlying mechanism is that higher porosity facilitates the diffusion of water molecules and other small species into the gasification fine slag, thereby increasing their physically adsorbed water content. This results in a reduction in the effective density of high-porosity materials during separation, approaching that of water, which leads to the preferential reporting of high-porosity fine particles to the concentrate. Consequently, the removal of these high-porosity fine particles represents a promising strategy for effectively reducing the ash content of the concentrate.

In summary, for the +0.125 mm gasification fine slag, particles characterized by high specific surface area, larger pore size, and high porosity tend to report to the concentrate, whereas those with low specific surface area, smaller pore size, and low porosity are directed to the tailings. For the 0.125–0.045 mm fraction, particles exhibiting higher specific surface area, larger pore size, and greater porosity enter the concentrate, while those with low specific surface area, larger pore size, and low porosity report to the tailings. In the case of the −0.045 mm fraction, particles with high specific surface area, smaller pore size, and high porosity are more likely to enter the concentrate, whereas those with low specific surface area, larger pore size, and low porosity report to the tailings. These

findings indicate that gasification fine slag with a high specific surface area and high porosity preferentially partitions into the concentrate, while that with low specific surface area and low porosity is more prone to reporting to the tailings. For the +0.125 mm and 0.125–0.045 mm fractions, materials with larger pore size exhibit a greater tendency to enter the concentrate. Conversely, for the −0.045 mm fraction, particles with smaller pore size are more likely to report to the concentrate. Therefore, regulating the content of −0.045 mm materials characterized by high specific surface area, high porosity, and small pore size constitutes the key to improving separation efficiency.

4.4. Analysis of the Mechanism of Pore Structure on Spiral Chute Separation of Gasification Fine Slag

The porous nature of gasification fine slag presents notable distinctions compared to conventional mineral separation processes. Porosity, specific surface area, and pore size distribution influence the settling behavior and migration trajectory of particles within the flowing film of the spiral chute by modifying their effective density. In this section, the effective density of particles with varying pore structures is calculated, and the regulating effect of porosity on vertical particle stratification is examined through the lens of the Bagnold effect. Furthermore, the correlation between pore structure and particle migration is established, elucidating the underlying mechanism by which pore structure governs the separation process.

4.4.1. Calculation of Effective Particle Density Based on Pore Water Adsorption

The effective density of particles, which arises from the adsorption of water within their pores when suspended in slurry, constitutes a fundamental parameter governing the forces acting upon them and their motion within the flowing film. In contrast to the true density or apparent density of solid materials, the effective density must account for the contribution of water adsorbed in the pore structure. The derivation of the formula for calculating effective density is presented as follows.

1. Calculation of Skeleton True Density

The true density of the particle skeleton is calculated based on the weighted average of the densities of carbon and ash components:

$$\frac{1}{\rho_{\text{solid}}} = \frac{1 - \frac{A_d}{100}}{\rho_{\text{char}}} + \frac{\frac{A_d}{100}}{\rho_{\text{ash}}} \tag{3}$$

where ρ_{solid} is the true density of the skeleton, g/cm^3. The density of residual carbon is ρ_{char}, g/cm^3. Generally, it is taken as 1.4 g/cm^3. The density of ash is ρ_{ash}, g/cm^3. The density of the ash fraction of gasification fine slag can be taken as 3.2 g/cm^3. From the formula, it can be seen that the higher the ash content, the higher the carbon skeleton density.

Based on literature reports [27,28], the average density of the raw gasification fine slag is approximately 2.3 g/cm^3. Given the fixed carbon content of 29.22% determined in this study and taking the density of the carbon rich component as 1.4 g/cm^3, the density of the ash bearing component is back-calculated to be in the range of 3.2 to 3.8 g/cm^3. Considering that the ash-bearing fraction in gasification fine slag predominantly exists in the form of an amorphous glassy phase with relatively low density, the average density of this fraction is estimated to be 3.2 g/cm^3 [29,30]. From the formula, it can be seen that the higher the ash content, the higher the carbon skeleton density.

2. Calculation of Porosity

The porosity ε is converted from the specific surface area data obtained by BET analysis.

$$\varepsilon = \frac{V_p}{V_p + \frac{1}{\rho_{\text{solid}}}} \tag{4}$$

where V_p is the pore volume per gram of gasification fine slag, in cm^3/g, and ρ_{solid} is the true density of the particle skeleton, in g/cm^3.

3. Effective Density of Gasification Fine Slag Considering Pore Water

The separation of gasification fine slag in a spiral chute is a wet separation process. During separation, the particles are fully immersed in water, and their internal pores become completely filled with water. The effective density is therefore defined as the total mass of the carbonaceous framework and the water contained within the pores, divided by the total particle volume. Accordingly, the effective density of gasification fine slag can be expressed by the following formula:

$$\rho_{eff} = (1 - \varepsilon) \times \rho_{solid} + \varepsilon \times \rho_{water} \tag{5}$$

where ρ_{eff} represents the effective density of particles in water (g/cm^3) and ρ_{water} represents the density of water, typically taken as 1.0 g/cm^3. It is evident from the formula that the effective density of gasification fine slag decreases upon the incorporation of adsorbed water.

The calculated effective densities for different particle size fractions of the separated products are presented in Figure 13.

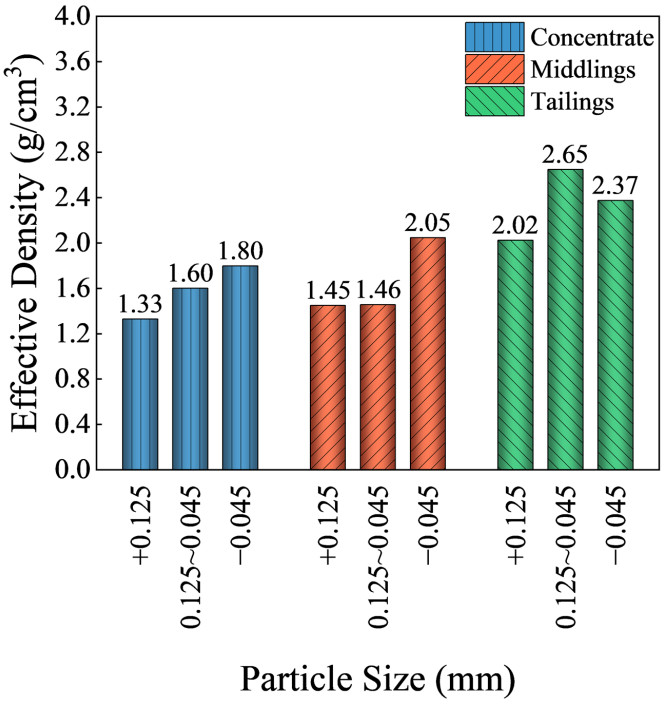

Figure 13. Effective density of separated products at different particle size fractions.

As shown in Figure 13, the effective density of products with different particle sizes presents a significant gradient distribution: concentrate < middlings < tailings. With decreasing particle size, the effective density of each product shows an increasing trend, reflecting the synergistic regulatory effect of pore structure and particle size on effective density.

The effective densities of different particle size fractions within each separated product exhibit marked differences. For the concentrate, the effective densities remained relatively

low overall and increased progressively with decreasing particle size. Specifically, the +0.125 mm fraction displayed the lowest effective density at 1.33 g/cm^3, followed by the 0.125–0.045 mm fraction at 1.60 g/cm^3, while the −0.045 mm fraction reached 1.80 g/cm^3. This trend suggests that concentrate particles consist primarily of highly porous residual carbon, where substantial pore water adsorption contributes to their reduced effective density. The slight increase in effective density observed in finer fractions is attributed to the higher proportion of mineral phases present.

The effective density of middlings products exhibits intermediate values, with a more pronounced particle size dependence. The effective density of the +0.125 mm and 0.125–0.045 mm fractions is identical at 1.45 g/cm^3, whereas that of the −0.045 mm fraction increases sharply to 2.05 g/cm^3. The middlings particles consist of a mixed carbon-mineral phase, and both their porosity and effective density lie between those of the concentrate and tailings. As particle size decreases, intensified mineral encapsulation causes the effective density of the fine fraction to approach that of the tailings.

The effective density of tailings products is generally high and exhibits an initial increase followed by a plateau as particle size decreases. The +0.125 mm fraction has an effective density of 2.02 g/cm^3, which increases to a peak value of 2.65 g/cm^3 for the 0.125~0.045 mm fraction, and then slightly decreases to 2.37 g/cm^3 for the −0.045 mm fraction. Tailings particles are predominantly composed of mineral phases with high ash content, resulting in low porosity and high effective density, which serves as the primary driver for their preferential migration into the tailings stream.

For a given particle size fraction, the effective density increases progressively from concentrate to middlings to tailings, and this density differential serves as the fundamental driving force underlying particle stratification and migration. In the +0.125 mm fraction, for instance, the effective density of the tailings (2.02 g/cm^3) is 0.54 g/cm^3 higher than that of the concentrate (1.33 g/cm^3), providing the density differential necessary to achieve efficient carbon–ash separation for this size fraction.

As particle size decreases, the effective density of each product increases. However, the gradient in effective density across products diminishes for the fine −0.045 mm fraction, with concentrate at 1.80 g/cm^3, middlings at 2.05 g/cm^3, and tailings at 2.37 g/cm^3, thereby weakening the density-driven separation mechanism. This reduced density differential is a key factor contributing to the poor separation efficiency observed for the −0.045 mm particle size.

4.4.2. Analysis of the Mechanism of Pore Structure on Spiral Chute Separation

Based on the aforementioned experimental findings, the presence of +0.125 mm coarse particles in the tailings stream contributes to a reduction in carbon recovery, a phenomenon associated with the Bagnold effect [31]. The +0.125 mm gasification fine slag preferentially reports to the concentrate product at the highest rate, while exhibiting a lower tendency to partition into the tailings. Therefore, elucidating how the porous structure of gasification fine slag influences its movement and stratification within the spiral chute is essential to further enhance carbon–ash separation efficiency.

During spiral separation, the elevated slurry concentration on the chute surface not only alters the configuration of the flowing film but also amplifies the Bagnold effect. First described by Bagnold in 1954 [27], this effect refers to the generation of a dispersive pressure perpendicular to the direction of shear when particles in suspension are subjected to continuous shearing, prompting lateral particle migration. This dispersive pressure increases with the velocity gradient. When the velocity gradient becomes sufficiently large for the dispersive pressure to counterbalance the effective gravitational force acting on the particles within the medium, the particles become suspended. The Bagnold effect plays

a significant role in promoting vertical stratification of particles in spiral separators [28]. In regions dominated by inertial collisions, characterized by a high particle Reynolds number, substantial dispersive pressure *P*a (N/m^2) and shear stress *T* (Pa) develop between particles [29]. The high concentration zone at the bottom of the spiral chute, where strong shearing forces are present, can be considered a region governed by inertial collisions.

$$P = a_i \rho_p (\lambda D)^2 \left(\frac{du}{dy}\right)^2 \cos \alpha_i \tag{6}$$

$$T = P \tan \alpha_i = a_i \rho_p (\lambda D)^2 \left(\frac{du}{dy}\right)^2 \sin \alpha_i \tag{7}$$

where ρ_p is particle density (kg/m^3), a_i is the experimental constant, which *Bagnold* (1954) takes as a value of 0.042, λ ($\lambda = D/s$) is linear concentration (dimensionless) reflecting the density of the reaction particle group, *D* is particle diameter (m), $\frac{du}{dy}$ is shear rate (s^{-1}), and α_i is particle collision angle (°), with its tangent value approximately 0.32 in the inertial region.

Termini et al. [30] noted that the equivalent density is a key parameter in the application of the Bagnold theory, as it comprehensively reflects the influence of both the particle framework and the internal fluid on the inertial mass. In the wet separation environment, the porous structure of gasification fine slag results in pores being filled with adsorbed water; consequently, the density governing their motion behavior corresponds to the effective density defined previously. Accordingly, the formula is revised as follows:

$$P = a_i \rho_{eff} (\lambda D)^2 \left(\frac{du}{dy}\right)^2 \cos \alpha_i \tag{8}$$

$$T = a_i \rho_{eff} (\lambda D)^2 \left(\frac{du}{dy}\right)^2 \sin \alpha_i \tag{9}$$

From the above formula, it can be seen that the dispersed pressure (*P*) and the effective density (ρ_{eff}) are proportional. That is, under the same shear environment, particles with higher effective density (ash rich) experience stronger dispersed pressure, while particles with lower effective density (residual carbon) experience weaker dispersed pressure.

The force analysis of the movement of gasification fine slag particles in a spiral chute shows [32] that by neglecting the particle acceleration term, the force balance equations of the particle in the tangential, normal, and oblique normal directions can be established:

$$G \sin \beta \sin \alpha + F_d \cos \delta - F_f - F_c \cos \beta \sin \alpha = 0 \tag{10}$$

$$F_N = G \cos \beta + F_c \sin \beta - F_l \tag{11}$$

$$G \sin \beta \cos \alpha - F_d \sin \delta - F_c \cos \beta \cos \alpha = 0 \tag{12}$$

Substituting the dispersive pressure relationship into the force balance equations and introducing the effective density (ρ_{eff}) in place of the intrinsic particle density, the relationship between the radial equilibrium position r of a particle and its material properties after separation can be derived as follows:

$$\frac{\rho_{eff} - \rho_l}{\rho_l} = \frac{1.5 h_m \sin \alpha}{D} \times \frac{k \tan \phi + \cos \delta + \sin \delta \tan \alpha + \sin \delta \tan \phi \tan \beta \sec \alpha}{\cos \beta + \sin \beta \tan \beta} \tag{13}$$

where ρ_l is fluid density (kg/m^3), h_m is average flow film thickness (m), α is longitudinal inclination angle (°), β is lateral inclination angle (°), δ is traction direction angle (°), k is normal traction coefficient t(°), and ϕ is particle internal friction angle (°).

As indicated by the derived relationship, for a given spiral chute configuration, the radial equilibrium position of a particle is determined solely by its effective density (ρ_{eff}) and particle size D.

When the particle diameter D approaches zero, fine particles are unable to establish a stable radial equilibrium position within the flow film. From a force analysis perspective, the mass of fine particles is negligible, rendering gravitational and centrifugal forces insignificant. Their motion is governed almost entirely by fluid resistance and turbulent diffusion, with trajectories closely following the fluid streamlines. Consequently, regardless of their effective density, fine particles are readily transported by secondary circulation toward the periphery, where they report to the concentrate and contribute to high-ash fine particle contamination. This mechanism explains the elevated ash content of 76.35% observed in the -0.045 mm fraction of the concentrate, which significantly compromises the quality of the coal product.

For particles larger than +0.125 mm in gasification fine slag, porosity governs the radial equilibrium position by modulating the effective density. Particles with high effective density (ash rich) report to the tailings, whereas those with low effective density (carbon rich) report to the concentrate, achieving effective separation. In contrast, for the -0.045 mm fine fraction, the particle size effect predominates and masks the influence of pore structure. Particle motion in this size range is governed primarily by fluid mechanics, resulting in the entrainment of high-ash fine particles into the concentrate and consequent contamination.

Therefore, optimization of the separation process for gasification fine slag should prioritize the control of fine particle fractions. This may be achieved through measures such as pre-desliming or adjusting operating parameters to mitigate the intensity of secondary circulation.

5. Conclusions

This study systematically investigated the separation performance of a spiral chute for carbon and ash from coal gasification fine slag, elucidated the migration behavior of particles with porous structures during flowing film separation, and established a mechanistic model based on effective density. The main conclusions are as follows:

(1) The spiral chute was applied to the carbon–ash separation of gasification fine slag, systematically revealing the synergistic effects of feed concentration and flow rate on separation performance. This implies that feed concentration and flow rate must be jointly optimized in industrial applications; a feed concentration of 10% combined with a flow rate of 1.96 m^3/h is recommended for the tested spiral chute configuration.

(2) The migration mechanism of porous particles within the flowing film is analyzed, suggesting that pore structure plays a key role in governing radial particle distribution by modulating effective density. Particles with high porosity preferentially report to the concentrate due to reduced effective density after water absorption. This suggests that feed materials with higher porosity are inherently more amenable to spiral separation due to their reduced effective density, providing a basis for feedstock pre-evaluation prior to separation.

(3) A separation model for porous particles was established based on the Bagnold effect and force balance analysis, revealing that the radial equilibrium position is co-determined by particle size and effective density, and identifying fine particle entrainment as the primary factor limiting separation precision. This indicates that improving

separation precision requires either pre-desliming to remove the −0.045 mm fraction or adjusting operating parameters to reduce secondary circulation intensity.

(4) The correspondence between morphological characteristics and separation behavior across different size fractions was revealed, indicating that −0.045 mm fine particles, dominated by mineral microspheres with underdeveloped pores, are difficult to separate effectively, providing a theoretical basis for process optimization. In practical flowsheets, the −0.045 mm fraction should be removed prior to spiral separation to avoid concentrate contamination and improve overall carbon recovery.

Author Contributions: Conceptualization, L.L. and L.H.; methodology, L.H.; software, L.H.; validation, L.L., L.H. and S.C.; formal analysis, L.H.; investigation, L.H., Y.L., Y.Y. and B.H.; resources, L.L., Z.L. and N.Z.; data curation, L.H.; writing—original draft preparation, L.H.; writing—review and editing, S.C. and W.Y.; visualization, L.H.; supervision, L.L., Z.L. and N.Z.; project administration, L.L.; funding acquisition, L.L. All authors have read and agreed to the published version of the manuscript.

Funding: This research was funded by the Natural Science Basic Research Plan in Shaanxi Province of China, grant number 2025JC-YBMS-398. The APC was funded by the corresponding authors.

Data Availability Statement: The original contributions presented in this study are included in the article. Further inquiries can be directed to the corresponding author.

Acknowledgments: The authors gratefully acknowledge the support and encouragement from all members of the research group, as well as the technical assistance provided by the laboratory staff.

Conflicts of Interest: The authors declare no conflicts of interest.

References

1. Mao, L. Characteristics of Fluidized Bed Gasification Fine Slag and the Mechanism of Carbon and Ash in Slag. Anhui University of Science and Technology, Huainan, China, 2023.
2. Yuan, H.H. Intrinsic Characteristics and Application Foundation Research of Coal Gasification Slag. Xi'an University of Architecture and Technology, Xi'an, China, 2020.
3. Ren, L.; Ding, L.; Guo, Q.; Gong, Y.; Yu, G.; Wang, F. Characterization, carbon-ash separation and resource utilization of coal gasification fine slag: A comprehensive review. *J. Clean. Prod.* **2023**, *398*, 136554. [CrossRef]
4. Matjie, R.H.; Van Alphen, C. Mineralogical features of size and density fractions in Sasol coal gasification ash, South Africa and potential by-products. *Fuel* **2008**, *87*, 1439–1445. [CrossRef]
5. Yang, Z.; Huang, G.; Zhao, Y.; Wang, L.; Sun, X.; Liao, Y.; Cui, X. Flotation and Mechanism of Oil Collector for Fine Slag from High Ash Coal Gasification. *Clean Coal Technol.* **2024**, *30*, 142–153. [CrossRef]
6. Xue, Z.; Dong, L.; Fan, M.; Yang, H.; Liu, A.; Li, Z.; Bao, W.; Wang, J.; Fan, P. Enhanced flotation mechanism of coal gasification fine slag with composite collectors. *Colloids Surf. A Physicochem. Eng. Asp.* **2022**, *641*, 128593. [CrossRef]
7. Liu, D.; Wang, W.; Tu, Y.; Ren, G.; Yan, S.; Liu, H.; He, H. Flotation specificity of coal gasification fine slag based on release analysis. *J. Clean. Prod.* **2022**, *363*, 132426. [CrossRef]
8. Guo, F.; Zhao, X.; Guo, Y.; Zhang, Y.; Wu, J. Fractal analysis and pore structure of gasification fine slag and its flotation residual carbon. *Colloids Surf. A Physicochem. Eng. Asp.* **2020**, *585*, 124148. [CrossRef]
9. Wang, Z.; Chang, Y.; Zhang, W.; Wang, C.; Liang, A. Gas-liquid flow characteristics of spiral separators with different downward bevel angles. *Phys. Fluids* **2025**, *37*, 093376. [CrossRef]
10. Arnold, D.J.; Stokes, Y.M.; Green, J.E.F. Particle-laden thin-film flow in helical channels with arbitrary shallow cross-sectional shape. *Phys. Fluids* **2019**, *31*, 073305. [CrossRef]
11. Li, Y. Research on the Optimization of Coal Slime Separation Process and Technical Transformation of Huangling No.1 Coal Preparation Plant. Xi'an University of Science and Technology, Xi'an, China, 2017.
12. Gao, S.; Meng, L.; Zhou, X.; Song, Z.; Zhou, S. The influence of feeding parameters on the spreading and particle separation behavior in the internal flow layer of a spiral chute. *Nonferrous Met. (Ore Dress. Part)* **2022**, *5*, 137–143, 158. [CrossRef]
13. Wang, Z.; Li, X.; Gao, S.; Zhai, D.; Zhang, G.; Ge, J. Research on the Application Effect of LXA1200 Spiral Separator. *Coal Process. Compr. Util.* **2023**, *8*, 54–58. [CrossRef]
14. Sadeghi, M.; Bazin, C.; Renaud, M. Radial distribution of iron oxide and silica particles in the reject flow of a spiral concentrator. *Int. J. Miner. Process.* **2016**, *153*, 51–59. [CrossRef]

15. Cui, S. Exploration of the Process for Recycling Nickel Metal from Flotation Plant Washing Water. *Metall. Eng.* **2009**, *29*, 46–49.
16. Wang, Q.; Gao, S.; Zhou, X.; Liu, C. Prediction of Spiral Chute Flow Field Evolution and Separation Indexes of Hematite and Quartz with Different Particle Sizes. *J. Northeast. Univ. (Nat. Sci. Ed.)* **2025**, *46*, 94–103. [CrossRef]
17. Meng, L.; Gao, S.; Zhou, X.; Wei, D. The influence of inlet flow on the evolution of the first circle flow field and mineral particle distribution in spiral chute. *J. Northeast. Univ. (Nat. Sci. Ed.)* **2023**, *44*, 856–862. [CrossRef]
18. Mahran, G. M. A.; Doheim, M. A.; AbdelGawad, A. F.; Abu-Ali, M. H.; Rizk, A. M. Numerical simulation of particulate-flow in spiral separators (15 % solids). *Afinidad* **2015**, *72*, 223–229. Available online: https://www.academia.edu/25674404/ (accessed on 20 August 2026).
19. Lee, S.; Stokes, Y.; Bertozzi, A.L. Behavior of a particle-laden flow in a spiral channel. *Phys. Fluids* **2014**, *26*, 043302. [CrossRef]
20. Yu, W.; Zhang, H.; Wang, X.; Rahman, Z.U.; Shi, Z.; Bai, Y.; Wang, G.; Chen, Y.; Wang, J.; Liu, L. Enrichment of residual carbon from coal gasification fine slag by spiral separator. *J. Environ. Manag.* **2022**, *315*, 115149. [CrossRef]
21. Lv, B.; Chai, X.; Deng, X.; Jiao, F.; Fang, C.; Xing, B. Recovery of residual carbon from coal gasification fine slag by a combined gravity separation-flotation process. *J. Environ. Manag.* **2023**, *348*, 119351. [CrossRef]
22. Zhu, R. An Investigation of Lignite-Based Carbon Materials and Their Adsorption Properties for CO_2. *Anhui Chem. Ind.* **2025**, *6*, 34–39. [CrossRef]
23. Chen, Y.; Zhang, Z.; Tang, C.; Zhang, H. Experimental Study on the Interaction between Coal Body Porosity Structure and High-Pressure CO_2 Adsorption. *J. Saf. Environ.* **2025**, *25*, 4577–4587.
24. Hu, Q.; Zheng, X.; Li, Q.; Zhang, Y.; Song, M.; Deng, Y. Porous Characteristics and Dynamic Wetting Behavior of Coal Particles with Different Particle Sizes. *J. Min. Saf. Eng.* **2024**, *41*, 1058–1068. [CrossRef]
25. Cao, T.; Song, Z.; Liu, G.; Yin, Q.; Luo, H. Nitrogen Adsorption Method—Mercury Porosimetry Analysis of Shale Pore, Fractal Characteristics and Their Influencing Factors. *Oil Gas Geol. Recovery Effic.* **2016**, *23*, 1–8.
26. Fang, K. Structure, Activity and Reaction Mechanism of Coal Gasification Slag and Its Composite Cementitious Material Properties. China University of Mining and Technology, Beijing, China, 2023.
27. Meng, L.; Gao, S.; Wei, D.; Zhao, Q.; Cui, B.; Shen, Y.; Song, Z. Particulate flow modeling in a spiral separator using the Eulerian multi-fluid VOF approach. *Int. J. Min. Sci. Technol.* **2023**, *33*, 251–263. [CrossRef]
28. Sudikondala, P.; Mangadoddy, N.; Kumar, M.; Tripathy, S.K.; Yanamandra, R.M. CFD Modeling of Spiral Concentrator- Prediction of Comprehensive Fluid Flow Field and Particle Segregation. *Miner. Eng.* **2022**, *183*, 107570. [CrossRef]
29. Bagnold, R.A. Experiments on a gravity-free dispersion of large solid spheres in a Newtonian fluid under shear. *Proc. R. Soc. Lond. Ser. A Math. Phys. Sci.* **1954**, *225*, 49–63. [CrossRef]
30. Termini, D.; Fichera, A. Experimental Analysis of Velocity Distribution in a Coarse-Grained Debris Flow: A Modified Bagnold's Equation. *Water* **2020**, *12*, 1415. [CrossRef]
31. Dehaine, Q.; Filippov, L.O. Modelling heavy and gangue mineral size recovery curves using the spiral concentration of heavy minerals from kaolin residues. *Powder Technol.* **2016**, *292*, 331–341. [CrossRef]
32. Chuan, Y. Research on the Flow Field Characteristics and Sorting Density Control of Spiral Separators. China University of Mining and Technology, Beijing, China, 2019.

Disclaimer/Publisher's Note: The statements, opinions and data contained in all publications are solely those of the individual author(s) and contributor(s) and not of MDPI and/or the editor(s). MDPI and/or the editor(s) disclaim responsibility for any injury to people or property resulting from any ideas, methods, instructions or products referred to in the content.